Microstructural evolution of the 21Cr32Ni model alloy under irradiation

M. Ayanoglu [*], A.T. Motta

Department of Mechanical and Nuclear Engineering, Pennsylvania State University, University Park, PA, 16802, USA

HIGHLIGHTS

- Microstructure evolution of ion irradiated 21Cr32Ni model alloy included the formation of loops, voids and caused irradiation induced segregation.
- Dual irradiation with He ions favored void and faulted loop formation.
- Faulted loop density increases with irradiation dose, while diameter decreases likely due to unfaulting.
- Voids are formed preferentially along grain boundaries and dislocations.
- Faulted loops become unfaulted during irradiation.

ARTICLE INFO

ABSTRACT

The microstructural evolution of the 21Cr32Ni model alloy under ion irradiation is investigated. A set of bulk materials were irradiated at the Michigan Ion Beam Laboratory using single beam (5 MeV Fe^{++}) to 1, 10 and 20 dpa at 440 °C and dual beam (5 MeV Fe^{++} plus energy degraded 1.95 MeV He^{++} ions) to 16.6 dpa at 446 °C. The average diameter and number density of the faulted loops and cavities formed under irradiation were characterized using Transmission Electron Microscopy (TEM). The behavior of faulted loop in the model alloy was also investigated in-situ using the Intermediate Voltage Electron Microscope (IVEM) at Argonne National Laboratory (ANL). Results show that the average faulted loop diameter decreases, but the faulted loop number density increases with increasing dose. In-situ experiments showed that the faulted loops become unfaulted during ion irradiation by interacting with network dislocations. Although the average faulted loop diameter after 16.6 dpa dual beam irradiation at 446 °C was found to be similar to those seen in samples irradiated with single beams to 10 and 20 dpa, the faulted loop number density was significantly higher in the dual beam irradiated sample. Moreover, the dual beam irradiated model alloy exhibits a significantly higher density of smaller cavities. It is also found that the size and density of the faulted loops and voids calculated for the dual beam irradiation of 21Cr32Ni model alloy at 446 °C are in better agreement with those measured in a sample neutron irradiated at 375 °C. Further discussion is presented in this study.

© 2018 Elsevier B.V. All rights reserved.

1. Introduction

Fast neutron irradiation of materials in nuclear reactors causes radiation damage in the form of displacement cascades through which a large number of defects and defect clusters, both interstitial and vacancy in nature, are created. At high irradiation temperatures some of these clusters are mobile; they can diffuse and form even larger clusters in the form of dislocation loops or cavities.

All these defect-defect and defect-sink interactions are at the root of 'microstructural evolution' which can alter the properties of the materials used in the reactor core. This issue is particularly important for the advanced reactor systems since in those systems, radiation damage levels can reach up to 200 dpa (displacement per atom) at operating temperatures of 400 °C or above [1]. Stainless steel alloys have been developed and improved to withstand in high temperature corrosion environments [2]. Because high dose neutron irradiation experiments require impractically long exposure times and can activate the irradiated samples, heavy-ion irradiation has been widely used to understand the effect of radiation on the materials behavior [3–9].

* Corresponding author.
E-mail address: mua214@psu.edu (M. Ayanoglu).

Alloy 800H (Fe-21Cr-32Ni) has been proposed as a candidate material for advanced reactor systems due to its high corrosion resistance [10]. Because of this, its microstructural changes under irradiation have been subjected to studies using both ions and neutrons. Gan et al. irradiated alloy 800H to 50 dpa using a single 5 MeV Ni ion beam at 500 °C. They observed faulted loops (average size of ~8.4 nm) and fine precipitates with an average size of ~6 nm and no void swelling [10]. Although the type of the precipitates are not reported, the authors reported that the average faulted loop number density increases with dose, whereas the average faulted loop diameter decreases. The absence of voids and the decrease in the average loop diameter were attributed by the authors to the formation of fine precipitates at elevated doses which might act as sinks for the point defects to recombine and alter the void and loop formation and growth [11,12]. Recently, Ulmer et al. investigated the behavior of alloy 800H under single beam irradiation of 5 MeV Fe ions at 440 °C up to 20 dpa and observed interstitial faulted loops [13]. The variation of faulted loop diameter and number density with irradiation dose reported by Ulmer et al. is consistent with that reported by Gan et al. However, they also reported the appearance of voids with average size of ~8–9 nm at 10 and 20 dpa, but not at 1 dpa. Tan et al. examined neutron irradiated samples of alloy 800H after 3 dpa at 500 °C at the Advanced Test Reactor (ATR) [14]. They also observed the development of faulted loops at 3 dpa but not at 1.3 dpa. This was attributed to the formation of $M_{23}C_6$ type and γ'-Ni_3(Ti, Al) type precipitates which served as sinks for the point defects which otherwise would cause loop nucleation and growth. The authors also reported the development of 30 nm diameter cavities after 1.3 dpa in contrast to what was reported for single beam irradiated alloy 800H [10,13]. The number density of the voids calculated for the neutron irradiated alloy 800H after 1.3 dpa at 500 °C is 10–100 times higher than that reported in 800H samples single Fe beam irradiated to 10 and 20 dpa at 440 °C [13].

All these studies provide valuable data on the behavior of alloy 800H under different irradiation conditions. However, there is clearly significant variation in the observations especially in the appearance of voids, their size and number density from one experiment to another. This poses the question of what we should be expected from after irradiation of austenitic steels intermediate to high doses where neutron irradiation data is scarce. The study of the neutron irradiated microstructure with ions requires that the latter to be benchmarked against neutron irradiation with careful characterization. To be able to reliably use ion irradiation as a surrogate for neutron irradiation, the ion irradiation experiments have to be performed taking into account the differences between ion irradiation and neutron irradiation [15–17].

The most significant difference may be the higher damage rate in ion irradiation experiments as compared to neutron irradiation. The ratio of the two damage rates can reach up to ~1000 [15]. Thus, although, the high damage rate is the whole reason to conduct ion irradiation experiments, it can also alter the relative balance between damage and annealing and lead to variations in microstructure evolution [16]. It has been proposed that the higher damage rates in self-ion irradiation experiments relative to neutron irradiation can be compensated by an increase in irradiation temperature and consequent higher annealing rate to match. The required temperature shift (ΔT) for a given dose rate can be obtained by using the invariance theory suggested by Mansur [18] based on the principle of obtaining the same total flow of defects to sinks in the two irradiations [15]. Was et al. demonstrated that the radiation induced segregation, radiation induced hardening and irradiation assisted stress corrosion cracking observed in neutron irradiated SS304 and SS316 type austenitic stainless steels at 275 °C up to 5 dpa can be successfully emulated using 3.2 MeV proton irradiations at 360 °C [19,20]. Similarly, Jiao et al. recently demonstrated that the dislocation loop microstructure observed in 304L SS and cold worked 316 SS irradiated to 46 dpa in BOR60 at 320 °C matches well the microstructure observed in the same alloys irradiated with a single beam of 5 MeV Fe++ or Ni++ to 130 dpa at 380 °C [15].

Another significant difference is that a neutron flux can generate helium from (n, α) reactions which is the absent in ion irradiation experiments. In nuclear reactors, helium generated from a series of transmutation reactions can promote void formation swelling and affect other aspects of irradiation induced microstructural evolution, such as dislocation mobility and precipitation [21–34]. Note that helium is much more effective at promoting voids than other residual gases, because it is insoluble at the temperatures of interest. Therefore, it can migrate and form bubbles which can then serve as nucleation sites for voids, thus increasing their concentration in the matrix. Farrell et al. reported that dual ion irradiation of SA 316 type austenitic stainless steel results in higher dislocation loop number density as compared to single beam irradiation [26]. He also reported that the helium can change precipitate chemical composition and retard radiation induced segregation in austenitic stainless steels.

The absence of gas in self-ion irradiation experiments requires simultaneous injection of helium during the ion bombardment to better simulate the reactor irradiation, as suggested by Mansur [17]. However, the temperature shift procedure is yet to be tested during dual ion irradiation.

In this paper, the microstructural evolution of the ternary alloy Fe21Cr32Ni (21 wt% of Cr and 32 wt% of Ni), which is the chemically analogous but compositionally simpler model alloy than alloy 800H is studied when subjected to both single beam (SB) and dual beam (DB) irradiation (5 MeV Fe++ and energy degraded 1.95 MeV He++ ions) with the application of temperature shift. The purpose of using a model alloy is to serve as reference to its analogues 800H and to provide a reference data for future modeling. Because alloying elements can have significant influence on microstructural evolution [8,35–37], it also allows us to discern understand the role of alloying elements on microstructure evolution in alloy 800H.

2. Experimental details

Bulk irradiated austenitic 21Cr32Ni alloys used in this study were provided by GE Global Research as heat # RAM-2192. Alloys were prepared from the original bulk material having 7.62 cm initial diameter and 1.84 cm initial thickness. A series of cold rolling processes at room temperature was applied to the original bulk material to reach an overall thickness reduction of 65%. The final heat treatment was conducted at 1200 °C for 2 h. The sample bars were then cut using an electrical discharge machine (EDM) to the dimensions of 20 mm × 1.5 mm × 1.5 mm as shown in Fig. 1. The surface of the alloys was mechanically polished to a 0.02 μm surface finish followed by electropolishing at approximately ~40 °C at 30V for 15 s using a 10% perchloric acid and 90% methanol solution prior to ion irradiation [15]. The elemental composition was measured by Sherry Laboratories (it is now known as "Element") using direct current plasma (DCP) emission spectroscopy as shown in Table 1. Note that the elemental compositions given in this table are bulk measurements which may vary slightly within the sample.

Bulk ion irradiations were performed in the Michigan Ion Beam Laboratory (MIBL) as a part of an Integrated Research Project (IRP) and also funded through the Nuclear Science User Facility Program [38,39]. The details of the bulk irradiation experiments performed at MIBL are described in detail by Taller et al. [38]. Three bars were single beam irradiated up to 1, 10 and 20 dpa at 440 °C and 1 bar
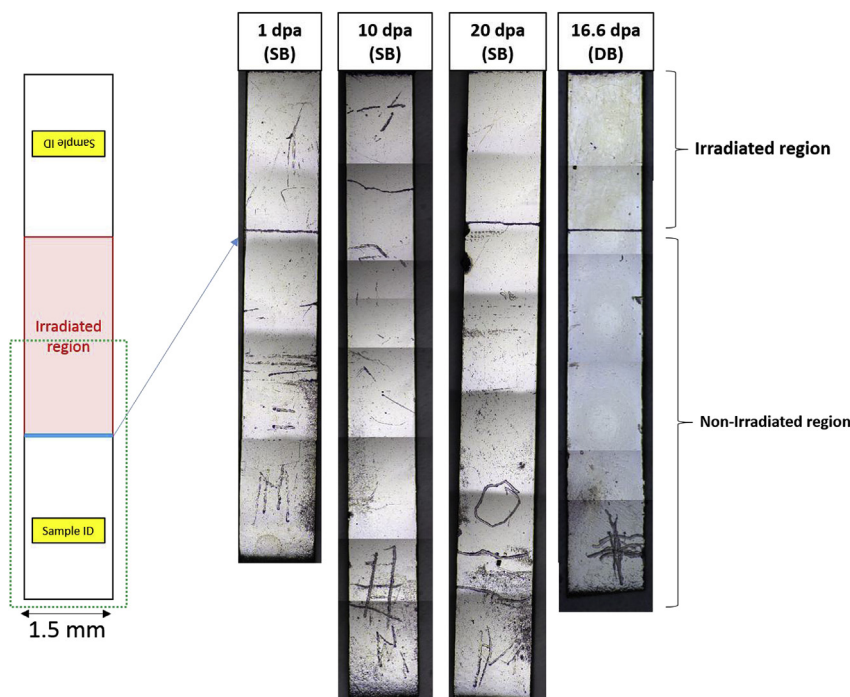
Fig. 1. Schematic illustration of 1.5 mm thick 21Cr32Ni model alloy bar is shown on the left. Optical microscope images shows half of the bars used for irradiations (from left to right: 1, 10 and 20 dpa single beam (SB) beam and 16.6 dpa dual beam (DB)). The irradiated regions for each sample are below the scratch indicated by the arrow.

Table 1
Bulk chemical composition of the major constituents of 21Cr32Ni model alloy measured by direct current plasma (DCP) method and commercial 800H.

Alloy	Fe	Ni	Cr	Mn	Other (Al, Ti, V, Cu, Si, Mo, P, C[a], S[a])
21Cr32Ni	Bal.	31.2	20.7	0.9	<0.2

[a] Combustion method (CO) used for carbon and sulfur measurement.

was irradiated to 16.6 dpa at 446 °C[1] using a dual beam with a corresponding damage rate of 5×10^{-4} dpa/s. Single beam irradiations were performed using 5 MeV Fe^{++}, while dual beam irradiations were performed with the simultaneous injection of energy-degraded 1.95 MeV He^{++} ions in addition to the 5 MeV Fe^{++} ions.

Because the damage rate under ion irradiation is much higher than that achieved in neutron irradiation ($\sim 10^{-7}$- 10^{-8} dpa/s), a temperature shift of $\Delta T = \sim 60$ °C was used to help compensate the high damage rates from the calculated BOR60 reactor irradiation temperature (~ 380°C-386 °C)[2]. This temperature shift is the same as used by Jiao et al. for self-ion irradiation of 304 and 316 type austenitic stainless steels [19]. The purpose for using 5 MeV ions (Fe^{++}) is to maximize ion flux through the accelerator leading to high dpa rates while avoiding significant changes in the Fe-Ni-Cr alloy composition. In addition, the 5 MeV iron ion irradiation affords a large damage depth allowing to characterize regions that are far from both the sample surface and the damage peak.

The damage profile for both single beam and dual beam irradiation was calculated using the SRIM code in Quick Kinchin Pease Mode with a displacement energy of 40 eV as suggested in Ref. [40].

The damage rate values are calculated at 600 nm depth, as indicated in Fig. 2. This depth was selected to minimize both surface effects and the injected interstitial effect [41]. For dual beam irradiation, helium implantation of 1 appm per dpa was extended to 300—1000 nm such that the He concentration profile in the target closely follows the ion damage curve, as illustrated in Fig. 2. The overall range of ions in the Fe21Cr32Ni target was found to be at ~2 μm and the peak dose was located at ~1.3 μm.

The irradiated microstructures were examined using transmission electron microscopy (TEM). TEM specimens were prepared using focused ion beam (FIB) performed in an FEI Helios Nano-Lab660 using 30 kV, 5 kV and 2 kV final polishing steps to minimize FIB induced damage [42]. An effort was made to lift out FIB samples close to grain boundaries to be able to investigate elemental segregation behavior using Energy Dispersive X-ray Spectroscopy (EDS) with FEI Talos TEM. The counting times in these experiments were ~20 min for each case and only a single grain boundary was examined in each sample. Foil thicknesses were determined using both Convergent Beam Electron Diffraction (CBED) and Electron Energy Loss Spectroscopy (EELS). The CBED patterns were obtained from the non-irradiated area, just beyond the ion range, to avoid the disruption that high levels of damage can cause on the CBED patterns. Cavities were imaged in the TEM by tilting the sample to a weak diffraction condition and recording bright-field images. The images were then merged together for quantification and comparison. The cavity diameter was measured from the inner ring of the dark fringe using underfocus bright field images. Faulted loop analysis was performed using the rel-rod dark field technique. The {111}-type faulted loops were imaged edge-on to facilitate quantification. To investigate the behavior of the faulted loops under irradiation, additional in-situ experiments were performed using the Intermediate Voltage Electron Microscope (IVEM) Facility at Argonne National Laboratory. At this facility, in-situ irradiation experiments were performed using 1 MeV Kr^{++} with the ion flux adjusted to give a damage rate of $(5-10) \times 10^{-4}$ dpa/s, similar to

---

[1] There is no specific reason for the 6 °C temperature difference between single and dual beam irradiation. 440 °C was the initial estimation of a temperature for ion irradiation experiments based on the proposed BOR-60 temperatures (380 °C) and invariance theory for a temperature shift. After we were informed that the temperature was slightly higher for the BOR-60 samples (386 °C), the dual beam ion irradiation temperature was increased accordingly.
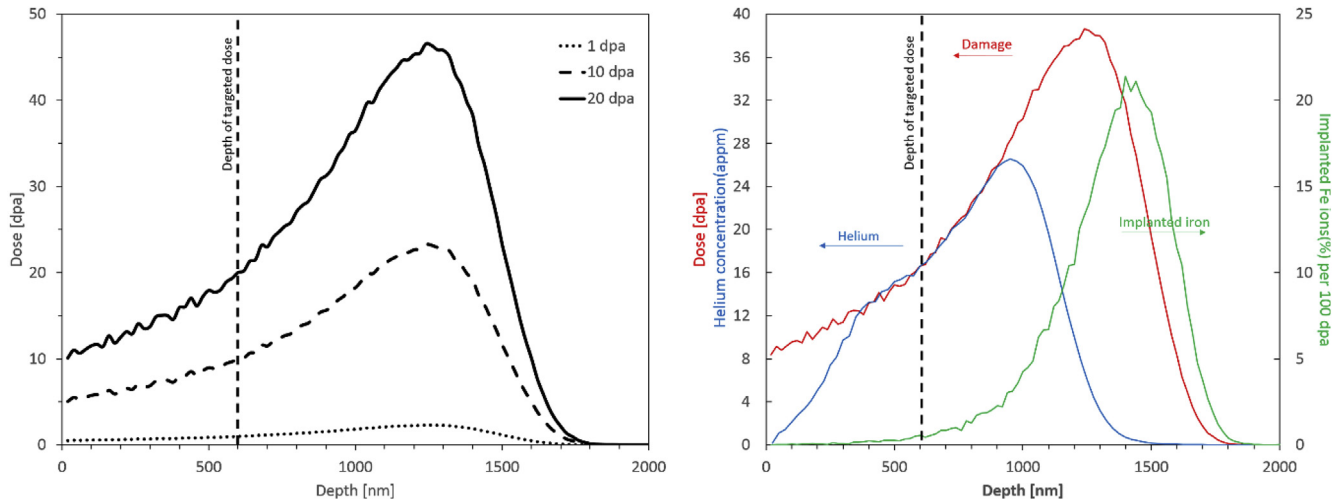
Fig. 2. The SRIM calculated damage profiles of 5 MeV Fe^{++} in 21Cr32Ni model alloy irradiated to 1, 10 and 20 dpa with single beam and 16.6 dpa with dual beam. The target dose in each case was achieved at 600 nm depth (dotted line). The helium implantation profile was provided by the Univ. of Michigan. (The damage produced by He is calculated to be 0.6% that of Fe and has consequently been neglected in these figures.)

that obtained in bulk ion irradiation at the specified depth. The in-situ ion irradiation was conducted at room temperature to avoid sample instability at high temperature and to provide relatively stable rel-rod dark field imaging conditions throughout the experiment.

The faulted loop density (ρ) was calculated from

$$\rho = \frac{N}{V} = \frac{N}{A \times \delta} \tag{1}$$

where N is the number of faulted loops counted in the TEM micrograph, and V is the characterized volume calculated from the surface area of the TEM image (A) and the measured thickness (δ). In a similar manner, the average faulted loop diameter (D_{ave}) and the average void diameter were calculated from

$$D_{ave} = \frac{1}{N} \sum_{i=1}^{N} D_i \tag{2}$$

where D_i is diameter of the individual faulted loop or void measured from the micrograph.

The errors in the determination of the faulted loop density and average faulted loop diameter are calculated by following the approach given in Ref. [13]. In this approach, the error for the faulted loop density (ε_ρ) was calculated by:

$$\varepsilon_\rho = \rho \sqrt{\left(\frac{\varepsilon_N}{N}\right)^2 + \left(\frac{\varepsilon_\delta}{\delta}\right)^2} \tag{3}$$

where ε_N is the counting error, $\sqrt{N}$, and ε_δ is the error of the thickness measurement, taken as 10% of the measured thickness. The error of the average faulted loop diameter (ε_D) is taken to be the standard error: $\sigma/\sqrt{N}$ where σ is the standard deviation of the measurement.

3. Results

The features observed in the 21Cr32Ni model alloy irradiated microstructures consist primarily of dislocation loops (most of which faulted in nature) and voids. In addition, chemical mapping recorded from the grain boundaries also shows radiation induced segregation in all irradiated samples.

The faulted loops and the voids are analyzed and presented in terms of their average diameter and number density, while RIS results are presented qualitatively with the chemical mappings obtained from the grain boundaries in each sample.

3.1. Dislocation loops

Fig. 3 shows cross-sectional bright field TEM images of the 21Cr32Ni model alloy microstructure after single beam irradiation to 1, 10 and 20 dpa at 440 °C and after dual beam irradiation to 16.6 dpa. The cross-section micrograph shown ranges from the outer surface (indicated with dashed lines in each case) to the end of the ion range. As seen in the figure, irradiation of the model alloy with 5 MeV Fe^{++} to 1 dpa results in a low density of relatively large dislocations loops (The average faulted loop diameter was ~25 nm). As the dose increases, the microstructure exhibits a high density of dislocation loops but with a smaller diameter (~14—16 nm) and a dense dislocation network, which creates a strong diffraction contrast in the corresponding bright field images, as shown in the bright field images taken at 10 and 20 dpa. A similar morphology microstructure including dislocation networks and small dislocation loops was observed in 16.6 dpa dual beam irradiated 21Cr32Ni microstructure, as shown in Fig. 3.

The habit planes of the dislocation loops observed in the ion irradiated microstructures of 21Cr32Ni have been identified as {110} type and {111} type. This is illustrated in Fig. 4 where two different {111} loop families are indicated with blue and yellow arrows, respectively while {110} type loops are indicated by red arrows. In each case (g, 4g) beam condition used for imaging is indicated by the white arrows. Corresponding rel-rod dark field micrographs recorded from the same region (Fig. 4b-c) show that the {111} type loops (imaged as edge-on) are faulted. The nature of these loops (i.e. interstitial or vacancy type) was not identified experimentally, but they are thought to be interstitial-type, based on similar studies performed on stainless steels, previously [43,44].

An analysis of the faulted loop distribution and the size distribution was performed to compare the microstructural evolution of this alloy after single beam and dual beam irradiation. Fig. 5 shows a series of rel-rod dark field micrographs recorded from the 500—700 nm depth region after irradiation to 1, 10 and 20 dpa with single beam and 16.6 dpa dual beam irradiation at ~440 °C, respectively. As seen in Fig. 5, both the loop number density and the
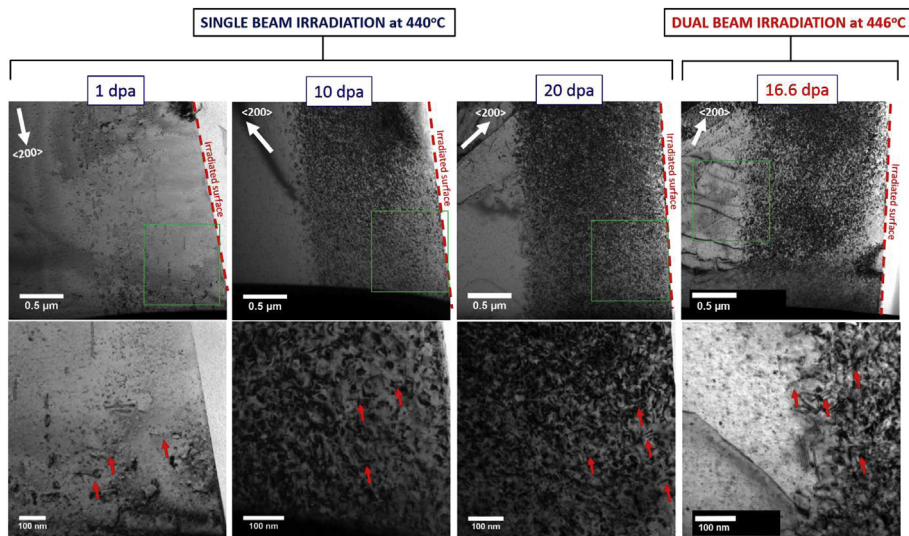
Fig. 3. Bright field images showing the microstructure of 21Cr32Ni model alloy after irradiation to 1, 10 and 20 dpa with single beam (5 MeV Fe^{++}) at 440 °C and 16.6 dpa with dual beam (5 MeV Fe^{++} and He^{++}) at 446 °C. Higher magnification images highlighted in the box at the top are shown at the bottom. In these micrograph some of the {111} type dislocation loops are seen as edge-on.
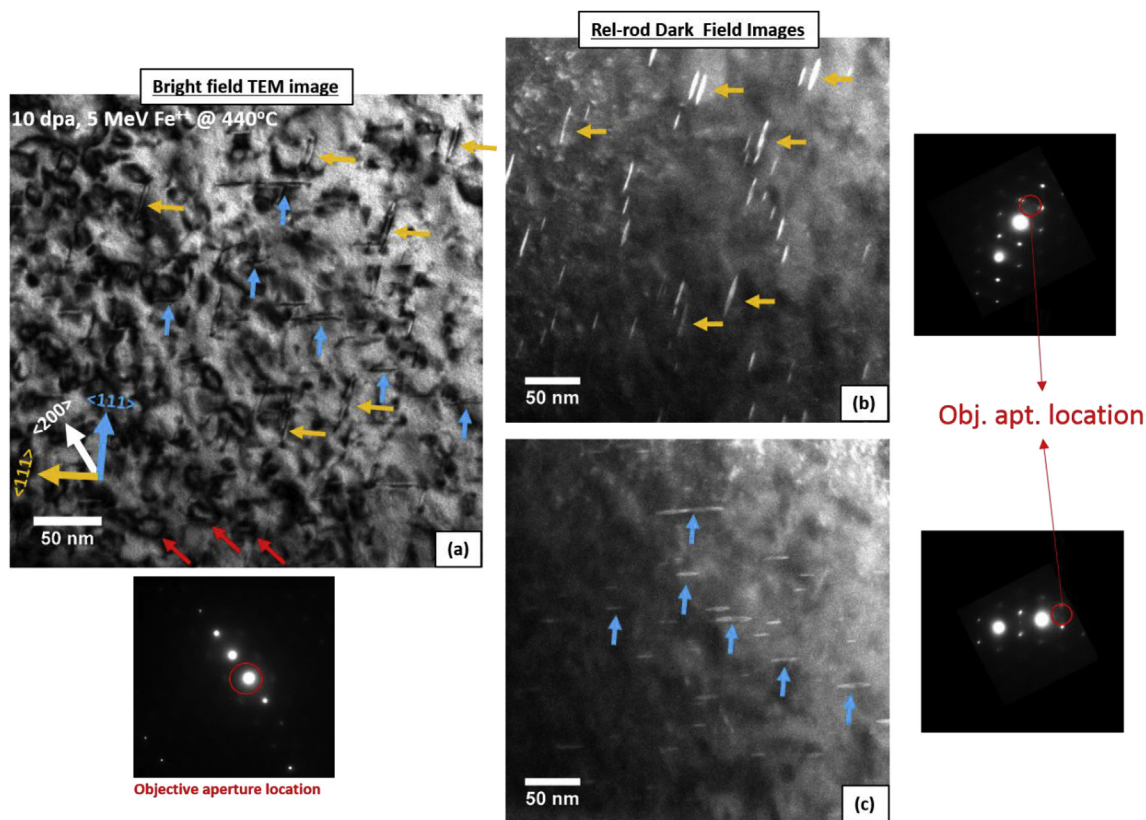

Fig. 4. (A) Bright field image showing {110} type (red) and {111} type (blue-yellow) dislocation loops observed in 10 dpa irradiated microstructure, **(b−c)** Rel-rod dark field images recorded from the same region show the two different variants of {111} type faulted dislocation loops. The location of the objective aperture in each condition is circled on the corresponding diffraction patterns. (For interpretation of the references to colour in this figure legend, the reader is referred to the Web version of this article.)

loop diameter change with increasing dose. The average faulted loop diameter and the number density determined from measurements performed on the 500−700 nm depth region in these micrographs are plotted in Fig. 6. Table 2 summarizes the same parameters for the entire irradiated region.

Fig. 6 shows that the measured average faulted loop diameter in single beam irradiated samples decreases with dose, approaching ~13−14 nm at 20 dpa. The corresponding faulted loop size distribution calculated for each microstructure with a large number of loops is shown in Fig. 7. The loop size distribution at 1 dpa is coarser than those seen at 10 and 20 dpa irradiated samples, reaching a maximum loop diameter of ~145 nm. For 10 and 20 dpa single
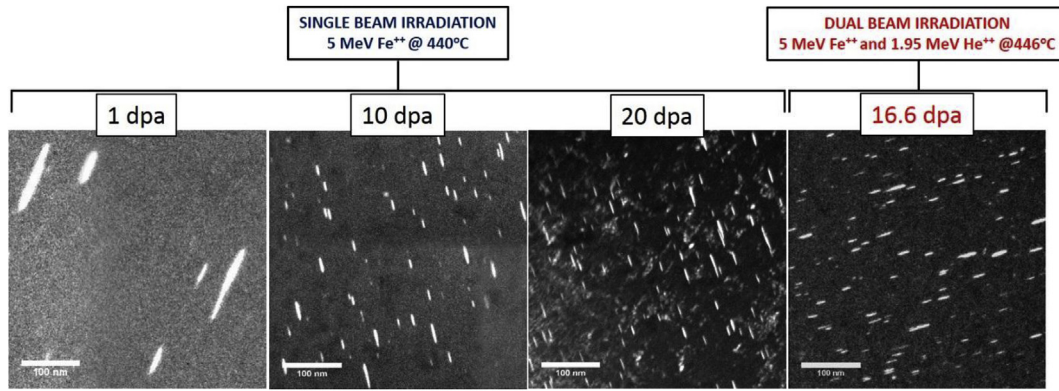
Fig. 5. Rel-rod dark field images showing faulted loop distribution (1/4 of total faulted loops) in 21Cr32Ni model alloy after the irradiation to 1, 10 and 20 dpa with single beam at 440 °C and to 16.6 dpa with dual beam at 446 °C. The bright spots observed in the 20 dpa irradiated microstructure are thought to be $M_{23}C_6$ type precipitates based on the corresponding diffraction pattern and they were excluded from the counting measurement. The scale bar is 100 nm.
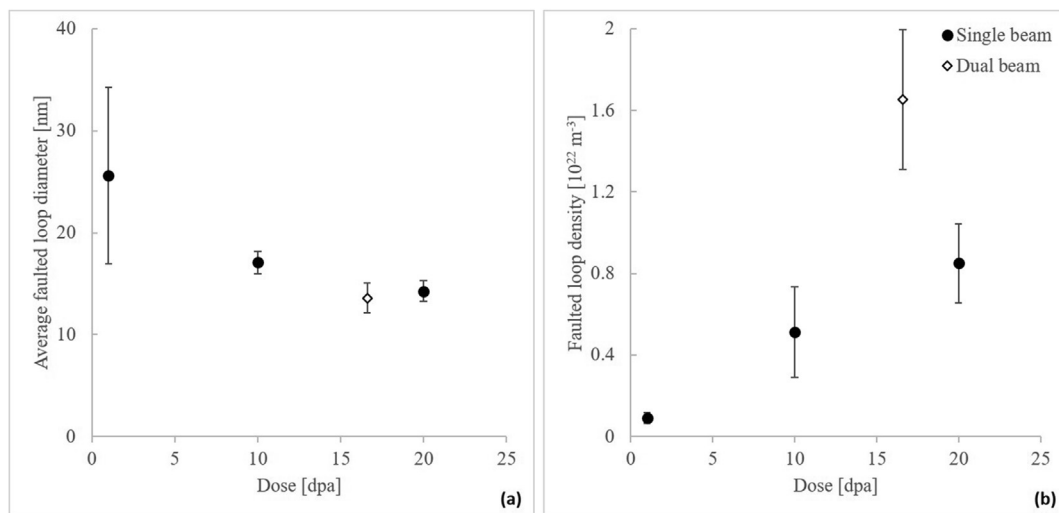

Fig. 6. (A) Average faulted loop diameter, and (b) average faulted loop density calculated at the 500−700 nm depth region in 21Cr32Ni austenitic model alloy microstructure irradiated to 1, 10 and 20 dpa single beam of 5 MeV Fe^{++} at 440 °C and 16.6 dpa dual beam of 5 MeV Fe^{++} and 1.95 MeV energy degraded He^{++} at 446 °C. Error bars are given as $\pm 2 \times$ (std. error). Corresponding average bin thicknesses are calculated as 89 nm, 203 nm, 179 nm and 105 nm. The thickness measurement error is assumed to be $\pm 10\% \times$ thickness.

Table 2
Faulted loop as a function of dose in 21Cr32Ni model alloy irradiated with 5 MeV Fe^{++} at 440 °C (500−700 nm depth).

Dose [dpa]	Irradiation condition	D_{ave} [nm]	ρ_{loop} [$\times 10^{22}$ m^{-3}][a]
1 dpa	Single beam at 440 °C	25.6 ± 8.7	0.09 ± 0.03
10 dpa		17.1 ± 1.1	0.51 ± 0.2
20 dpa		14.3 ± 1.0	0.85 ± 0.2
16.6 dpa	Dual beam at 446 °C	13.6 ± 1.4	1.65 ± 0.3

[a] Only 1/4 of the total loops were counted and results were multiplied with four.

beam irradiations, the loop size distributions are similar: they are narrower and shifted towards to smaller sizes relative to what is seen at 1 dpa. The faulted loop number density, however, increases with dose in the single beam irradiated microstructures. The calculated faulted loop densities at 10 and 20 dpa are approximately 5 and 10 times higher than those obtained at 1 dpa.

The average faulted loop diameter in the dual beam irradiated microstructure was found to be similar to that observed after 10 and 20 dpa single beam irradiation. On the other hand, a remarkable increment in the faulted loop number density is found in the sample dual beam irradiated to 16.6 dpa compared to both 10 and 20 dpa single beam irradiation.

3.2. Voids

Irradiation of the 21Cr32Ni model alloy with both single beam and dual beam resulted in the formation of voids as shown in Fig. 8. In the sample irradiated to 1 dpa with single beam, voids were homogenously distributed up to ~1400 nm depth, whereas they are only visible at beyond ~1400 nm depth in 10 and 20 dpa single beam irradiated samples as shown in Fig. 8c-e, where small voids are indicated with arrows as shown in Fig. 8d-f.

In the sample irradiated to 16.6 dpa with dual beam, a high density of smaller voids are homogenously distributed over a depth range of ~300−1200 nm from the outer surface. For this sample, no voids are observed beyond the ~1300 nm depth, which roughly corresponds to the ion implantation peak. In addition, the voids in the dual beam microstructure formed preferentially at the grain boundaries as shown in Fig. 9 with the voids highlighted in yellow in Fig. 9b. The pre-existing microstructure affects void nucleation: it is clear that the voids are more frequently observed along the grain boundaries. Also no voids were seen near the other surface (<100 nm) during bulk irradiation which is in agreement with the results in 800H [13].
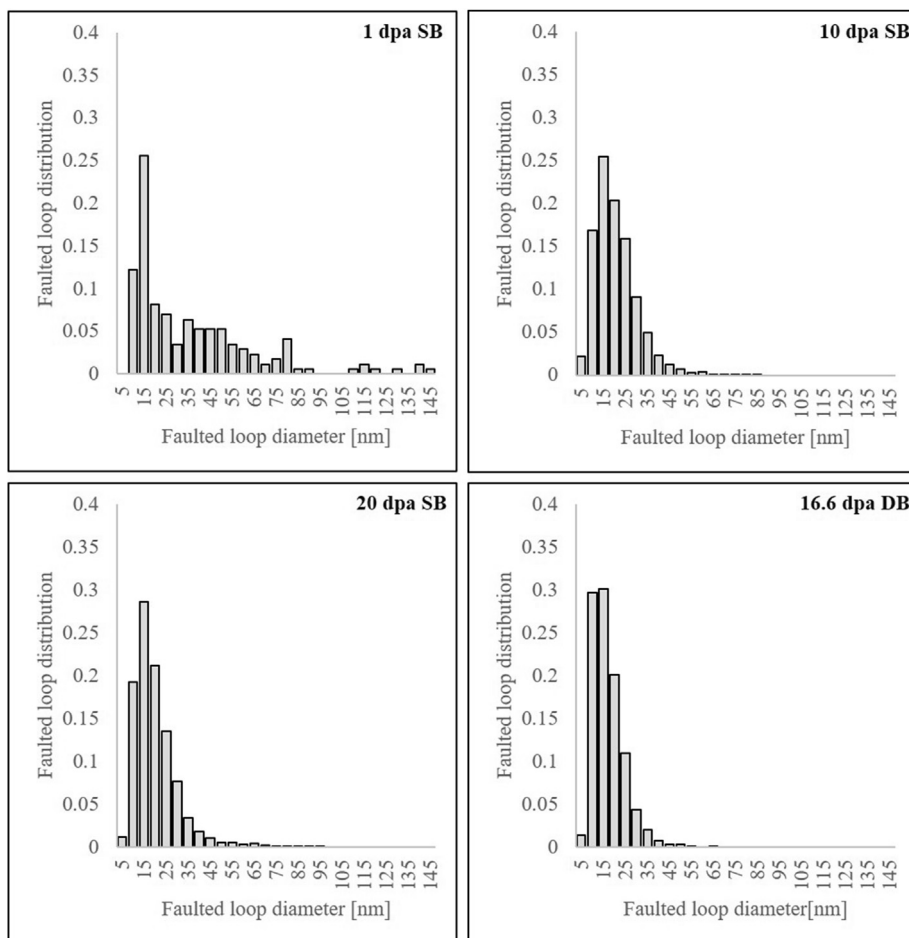
The calculated average void diameter is measured; and the

Fig. 7. Faulted loop diameter distribution in 21Cr32Ni model alloy after single beam irradiation to **(a)** 1 dpa at 440 °C, **(b)**10 dpa at 440 °C, **(c)**20 dpa at 440 °C and **(d)** dual beam irradiation to 16.6 dpa at 440 °C. The faulted loop size distribution shows bigger loops at low dose and a narrowing and shift towards smaller diameters at higher doses.

percent swelling, are plotted versus sample depth in Fig. 10 and Fig. 11. For these profiles, a 100 nm bin size was used from the surface to the total depth of ~2000 nm for each condition. The percent swelling for each bin was calculated using the following equation [45]:

$$S(\%) = \frac{\frac{\pi}{6}\sum_{i=1}^{N} D_i^3}{A_i \times \delta - \frac{\pi}{6}\sum_{i=1}^{N} D_i^3} \times 100 \qquad (4)$$

where D_i is the cavity diameter measured with ImageJ, N is the total number of voids counted in each bin, A_i is the bin area and δ is the sample average thickness (calculated with EELS) which was taken to be constant for each bin.

Fig. 10 shows that the average void diameter does not vary with depth in any of the irradiated microstructures examined. For the 1 dpa single beam irradiated microstructure, the average void diameter is calculated as 9.1 ± 2.4 nm. The latter is the standard error. As the dose increases to 10 dpa, the average void diameter decreases slightly to 5 ± 0.7 nm before increasing back again to 8.1 ± 0.9 nm at 20 dpa. The standard deviations for these measurements are ± 1.8 nm, ± 1.4 nm and ± 2.2 nm, respectively. If the model alloy is irradiated with the dual beam to 16.6 dpa, the average void diameter decreases to 4.2 ± 1.5 nm with a standard deviation of ± 0.5 nm. In fact, additional measurements using higher magnification images (>80kx) recorded from 500 to 700 nm depth region (see Fig. 8h) reveals that the average void diameter can be remarkably smaller

$(2 \pm 1.5$ nm with standard deviation of $\pm 0.7)$ than those given in Fig. 8g due to the contribution of the voids having diameter less then ~2 nm into the measurement. Note that these small voids are only visible at relatively high magnifications (>80 kx) and thus cannot be seen in the low magnification images shown.

The swelling depth profile (%) calculated for each microstructure is plotted in Fig. 11. For the 1 dpa single beam irradiated microstructure, less swelling was observed near the surface and close to the ion injected peak location with the maximum swelling seen at 500–700 nm. As the dose increases to 10 and 20 dpa, swelling is only observed beyond ~1400 nm. In addition, the overall amount of swelling observed in 10 and 20 dpa single beam irradiated microstructures is much lower compared to that observed after irradiation to 1 dpa.

The swelling depth profile observed in 16.6 dpa dual beam irradiated microstructure is similar to that seen after 1 dpa such that less swelling was observed near the sample surface and in the vicinity of the injected ion peak location. The overall swelling in dual beam irradiated microstructure was found to be significantly higher than in the sample irradiated under single beam as seen in Fig. 11.

3.3. Radiation-induced segregation at grain boundaries

Fig. 12 shows chemical mapping of the irradiated alloys collected by using EDS attached to a TEM from the region close to the 600 nm target depth. The average bulk composition is similar to
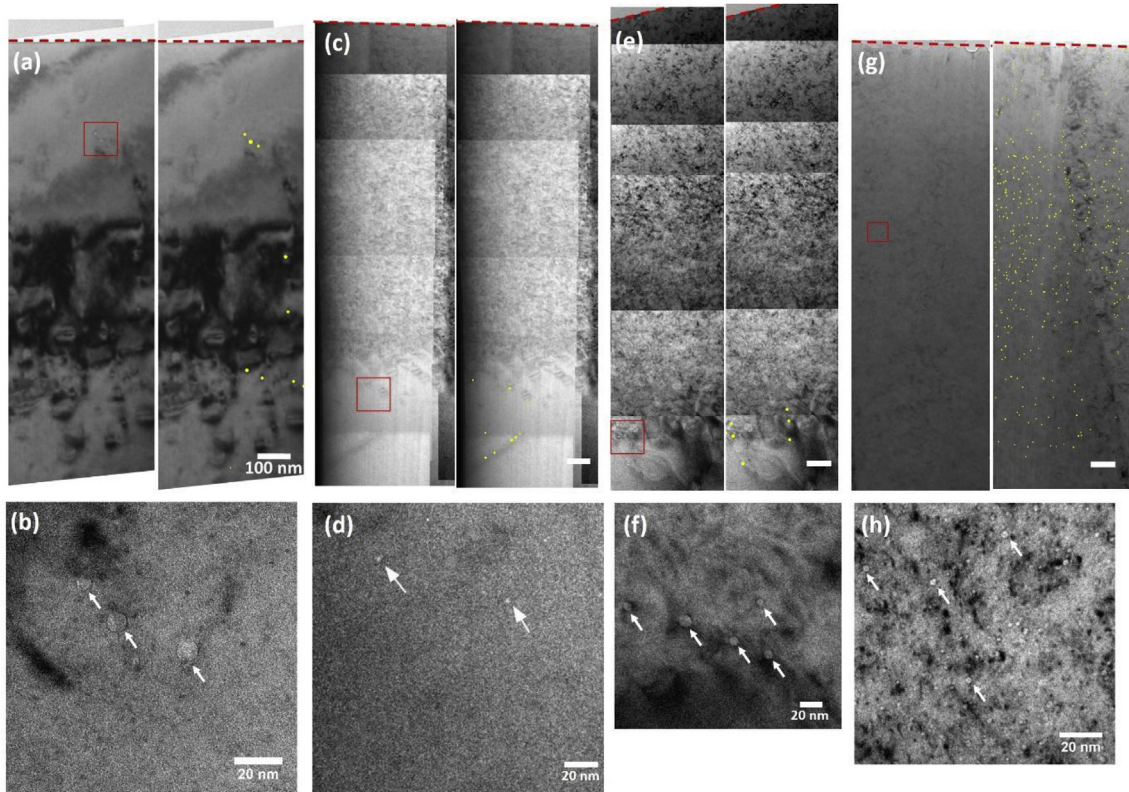
Fig. 8. Bright-field TEM micrographs showing the void distribution in 21Cr32Ni model alloy irradiated to (**a**–**b**) 1 dpa with single beam, (**c**–**d**) 10 dpa with single beam, (**e**–**f**) 20 dpa with single beam, and (**g**–**h**)16.6 dpa with dual beam. Higher magnification images corresponding to the boxes shown at the top are given at the bottom of each image. Single beam irradiations were performed at 440 °C with 5 MeV Fe^{++} and dual beam irradiations were performed with simultaneously injected 1.95 MeV energy degraded He^{++} at 446 °C. Some of the voids are highlighted as an overview for better visibility.
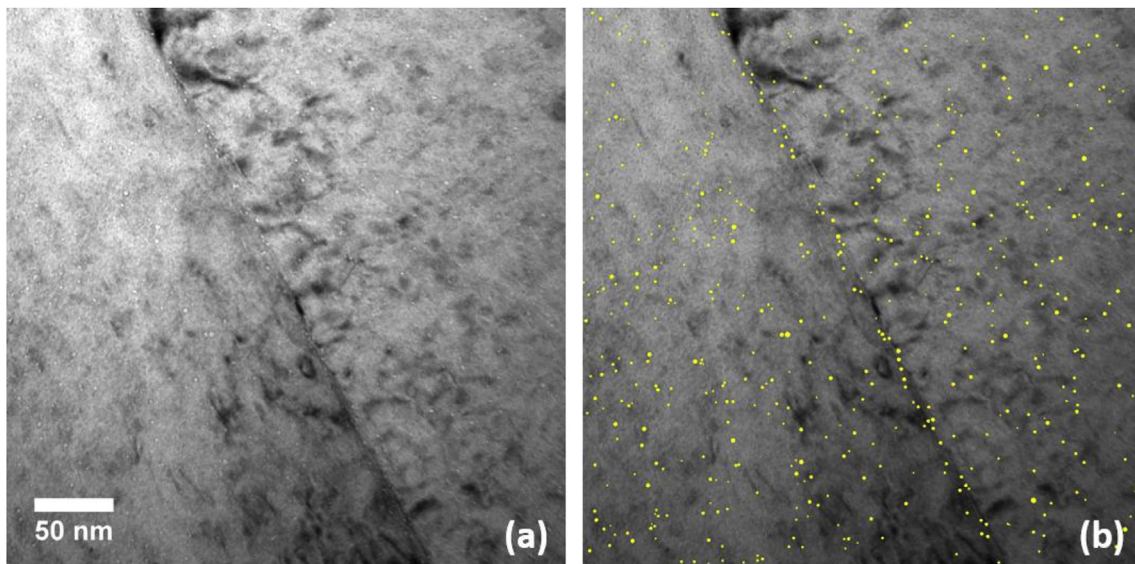

Fig. 9. (**A**) Dual-beam irradiated 21Cr32Ni model alloy microstructure showing more void formation along the grain boundary (**b**) Cavities are highlighted for better visibility.

the non-irradiated alloy composition given in Table 1. However, irradiation of the model alloy results in micro-chemical changes at the grain boundary as seen in Fig. 12. Irradiation of the model alloy even after 1 dpa with single beam results in Ni segregation and in Fe, Cr and Mn depletion. The degree of segregation seems to increase with dose as seen in Fig. 12 while the Ni signal looks sharper at higher doses.

4. Discussion

4.1. The evolution of the faulted loops in 21Cr32Ni model alloy

As mentioned previously, the average faulted loop diameter decreases and saturates with dose in the single beam irradiated microstructures, while the faulted loop number density increases,
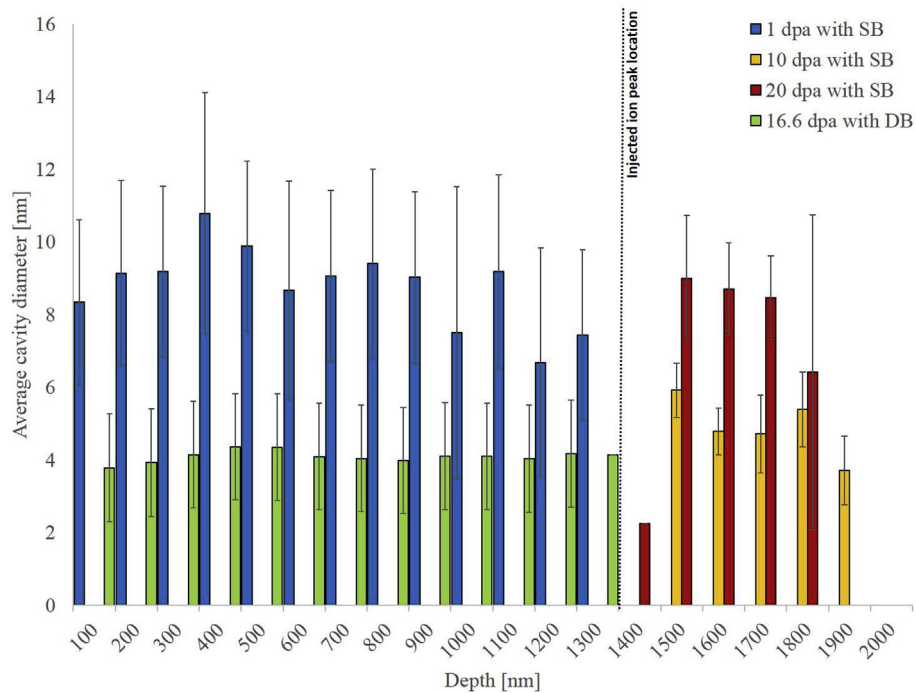
Fig. 10. Average void diameter depth profile of 21Cr32Ni model alloy irradiated with single beam of 5 MeV Fe^{++} at 440 °C to 1, 10 and 20 dpa and with dual beam of 5 MeV Fe^{++} and 1.95 MeV energy degraded He^{++} at 446 °C to 16.6 dpa. The corresponding average bin thicknesses are calculated as 89 nm, 203 nm, 179 nm and 105 nm. The thickness measurement error is assumed to be ±10% × thickness.
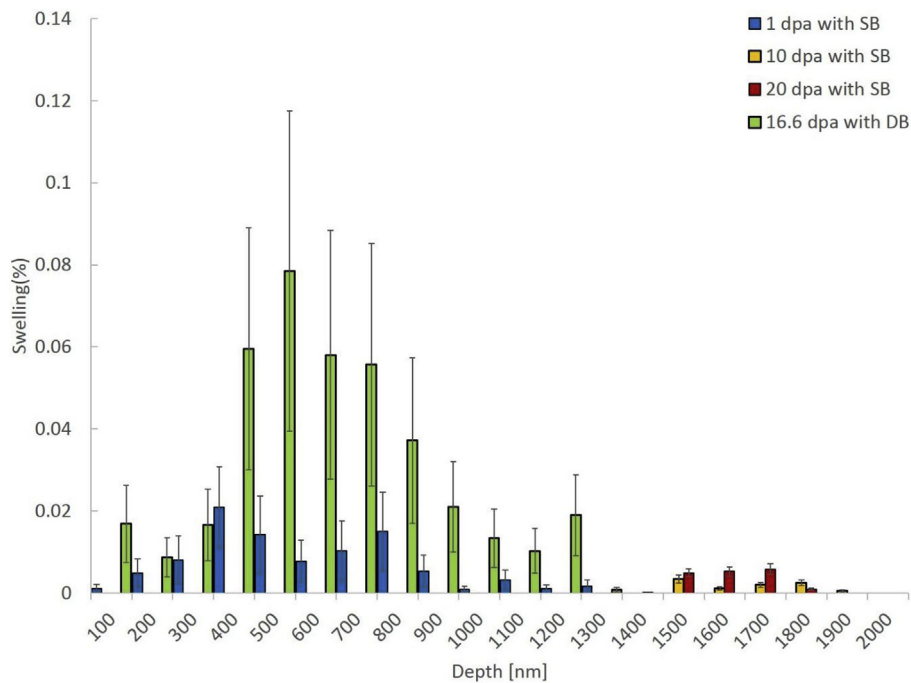

Fig. 11. Calculated swelling depth profile of 21Cr32Ni model alloy irradiated with single beam of 5 MeV Fe^{++} at 440 °C to 1, 10 and 20 dpa and with dual beam of 5 MeV Fe^{++} and 1.95 MeV energy degraded He^{++} at 446 °C to 16.6 dpa. The corresponding average bin thicknesses are calculated as 89 nm, 203 nm, 179 nm and 105 nm. The thickness error measurement is assumed to be ±10% × thickness.

as shown in Fig. 6. Even considering the large errors bars associated with the measurements, the results appear to indicate that the faulted loop number density saturates with dose. The observation of {110} type perfect loops along with the high dislocation density network structure and the absence of large faulted loops at elevated doses indicates that the larger loops become unfaulted through interaction with other dislocations. Recent molecular dynamics simulations performed on FCC metals and pure Ni have shown that
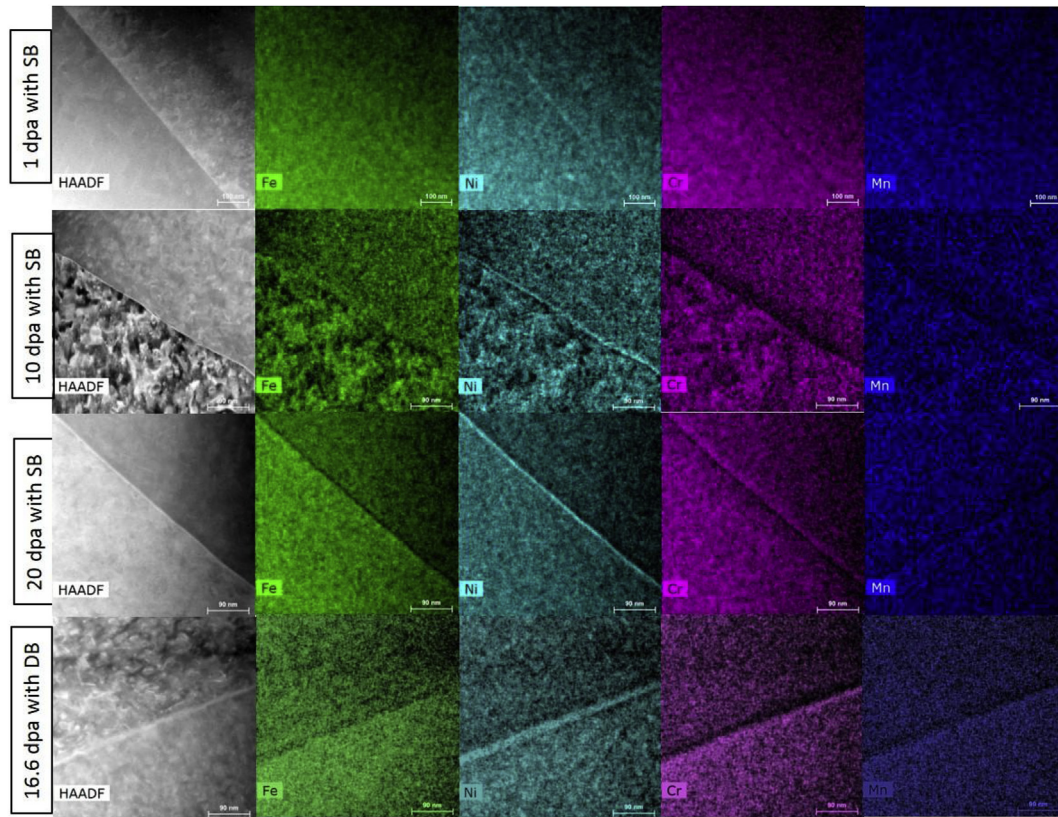
Fig. 12. Chemical mapping of 1, 10 and 20 dpa single beam and 16.6 dpa dual-beam irradiated 21Cr32Ni model alloy showing higher Ni segregation and Fe, Cr and Mn depletion along the grain boundary with increasing dose.

the faulted loops can become unfaulted through the formation of Shockley partials via the incorporation of dislocations [46—48]. Ulmer et al. recently reported a possible unfaulting process in alloy 800H after an additional dose of ~2—3 dpa [13].

To verify the unfaulting process experimentally, we used in-situ ion irradiation, using a rel-rod dark field technique to image the process of faulted loops in the 21Cr32Ni model alloy microstructure. For this particular experiment, an electron thin sample was prepared using FIB from the 1 dpa single beam bulk irradiated alloy and further irradiated at the IVEM facility with 1 MeV Kr^{++} using the similar damage rates (($\sim5{-}10) \times 10^{-4}$) at room temperature. Fig. 13 shows sequential video frames that capture the un-faulting process observed on the labeled faulted loops. The disappearance of the faulted loops from the rel-rod dark field images indicates that the faulted loops become unfaulted during the irradiation. The unfaulting starts after an additional in-situ dose of +0.23 dpa (1.23 dpa in total) with loop 'b' as indicated in Fig. 13. Further irradiation of 1 dpa pre-irradiated 21Cr32Ni sample results in unfaulting of additional faulted loops (see loops 'a' and 'c'). The unfaulting occurred as a result of interaction with a gliding dislocation across the faulted loop.

The required additional dose for loop unfaulting in the 21Cr32Ni model alloy is much lower than in the alloy 800H reported by Ulmer et al. (~+0.23 dpa vs ~+2 dpa). This indicates that the loops unfault more easily in the 21Cr32Ni model alloy than alloy 800H. This is also consistent with our TEM observations where many more {110} type unfaulted loops were observed in the irradiated 21Cr32Ni microstructure than in the analogous alloy 800H. Also, the faulted loop number densities obtained for the single beam irradiated 21Cr32Ni samples in this study are found to be lower than those reported for the single beam irradiated alloy 800H

samples by about a factor of ~2—3 [13]. The observation of a lower density of faulted loops in the model alloy than in 800H also suggests that loop unfaulting in 21Cr32Ni is energetically more favorable than in alloy 800H. In other words, unfaulting rate in the model alloy is expected to be higher which reduces the faulted loop number density. Because similar conditions were used during the irradiation of 21Cr32Ni model alloy and alloy 800H, this difference can be attributed to the existence of alloying elements in alloy 800H. It is possible that the additional alloying elements in alloy 800H are absorbed at dislocations, hampering their glide. Because unfaulting occurs through dislocation glide, this could reduce the unfaulting rate during irradiation and increase the faulted loop population in the alloy 800H.

There is no clear evidence showing that helium influences the dislocation loop diameter in irradiated 21Cr32Ni model alloy. Fig. 6a shows that the average faulted loop diameter after dual beam irradiation is similar to that of single beam. On the other hand, the helium injection does increase the faulted loop density. Fig. 6b shows that the faulted loop number density is a factor of 2 higher in the dual beam irradiated 21Cr32Ni microstructure than in the 21Cr32NI microstructure irradiated to 10 and 20 dpa with. This is thought to be due to enhanced void formation in the dual beam irradiated microstructure (see Fig. 8) resulting in an excess of interstitials available in the matrix to form loops.

4.2. The evolution of the voids in 21Cr32Ni model alloy

Void formation was observed in all samples examined in this study and found to occur preferentially at pre-existing dislocations and at the grain boundaries. Because dislocations and grain boundaries have more open atomic space than the bulk of the
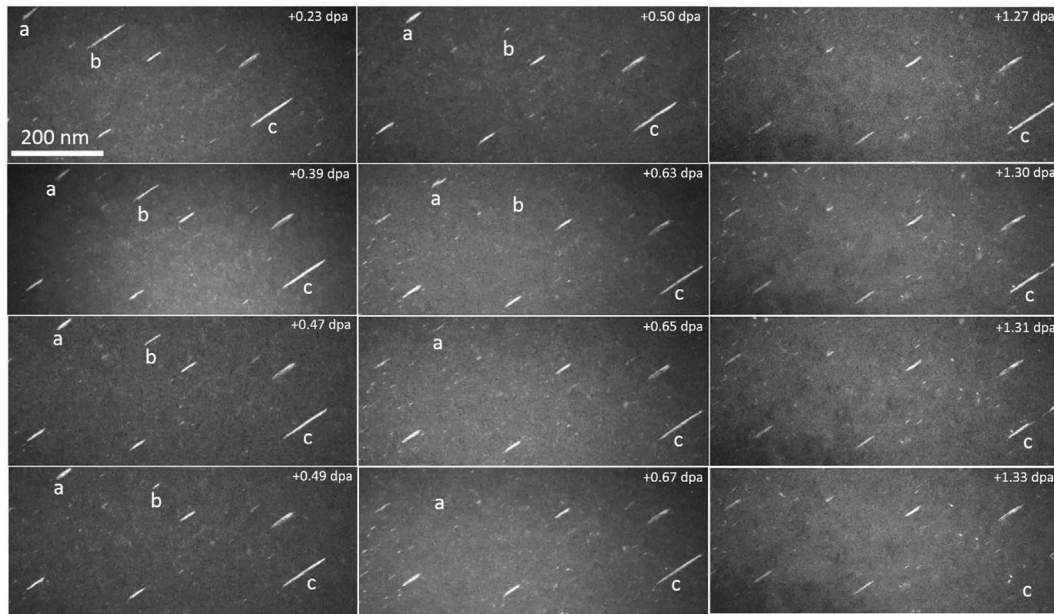
Fig. 13. Rel-rod dark field images showing the unfaulting process of different dislocation loops (labeled with a, b and c) during in-situ irradiation of 1 dpa pre-irradiated 21Cr32Ni model alloy at room temperature. In this sequence both 'a' and 'b' disappear as the observation proceeds.

material, they may act as preferential sites for the void formation. Also, very few voids were observed in all irradiated samples near the surface indicating that the sample surface is an effective sink for the defects at this temperature.

Fig. 11 shows that voids are observed in 21Cr32Ni irradiated at 440 °C to 1 dpa with single beam which was not reported after irradiating alloy 800H with single beam to 1 dpa at 440 °C and 5 dpa at 500 °C [10,13]. This indicates that void formation in the model alloy occurs earlier than in alloy 800H. This could be caused by a lower alloying elements content in the model alloy, as it is known that the oversize solutes (such as Nb, Ti etc. in alloy 800H) and undersize elements (such as Al, Si etc.) can trap vacancies and interstitials thus; enhancing their recombination and decreasing the nucleation of the voids [49,50].

As the dose increases to 10 and 20 dpa, the swelling profile shifts towards to the 1400−2000 nm depth region. The absence of voids in shallow region at 10 and 20 dpa single beam irradiated samples is unexpected, because voids were initially observed in that region after 1 dpa single beam irradiation (Fig. 8a). This suggests that the voids which were initially formed at early stage of irradiation (<1 dpa) disappeared afterwards with during the irradiation to the doses between 1 and 10 dpa.

Moreover, the voids observed after 10 dpa single beam irradiation are smaller (5.0 ± 0.7 nm) than those seen at 1 dpa sample (9.1 ± 2.4 nm) and tend to grow with the further irradiation to 20 dpa (8.1 ± 0.9). It is possible that these voids are newly formed as opposed to the ones observed in the shallow regions after 1 dpa and grow with bias-driven. The appearance of these voids only within 1400−2000 nm depth after 10 irradiation indicates that the injected interstitials are absorbed by the other sinks or diffuse to the other regions in the matrix rather than recombine with vacancies. However, the disappearance of the voids in shallow regions is still puzzling. One explanation could be that the injected interstitials diffuse to shallower regions such that the excess vacancies remain near the ion implanted region and form voids while voids in the shallow regions shrink because of the excess interstitial absorption.

To perform a quick feasibility check whether the injected ions are capable of suppressing void formation, the total number of vacancies associated with the voids is calculated and compared with the number of injected interstitials created. The total vacancy density ($N_{vacancy}$) cm^{-3} is calculated as:

$$N_{vacancy} = \frac{\frac{4}{3}\pi \overline{R}^3 C_{void}}{\Omega} \qquad (5)$$

where $\overline{R}$ is the average radius of the voids measured to be ~4.5 nm after 1 dpa irradiation, C_{void} is the corresponding void density taken as 1.4×10^{14} voids/cm^3, and Ω is the single vacancy volume taken as ~10^{-23} cm^3. Using this equation, the vacancy concentration associated with voids at 1 dpa is calculated as $N_{vacancy} = 5.5 \times 10^{18}$ vacancy/cm^3.

The total number of injected ions is simply the ion fluence, ϕt, required to reach to 10 dpa, which can be calculated as

$$\phi t = \frac{kt \times N_{at}}{v} \qquad (6)$$

where kt is 9 dpa (the additional dose added to the material to reach 10 dpa), N_{at} is the atomic number density in the alloy (~9×10^{22} atoms/cm^3), and v is the displacement/ion obtained from the SRIM output file. Using eq. (6), the total ion fluence to deliver 9 dpa is calculated as ~2.5×10^{16} ions/cm^2.

By integrating the ion implantation profile given in Fig. 2 (green line) and multiplying the ion fluence, the total injected interstitial concentration is calculated as $N_{injected} = $~$1 \times 10^{22}$ ions/cm^3. Comparing the two numbers $N_{injected}$ is 4 orders of magnitude higher than $N_{vacancy}$ so that even if, 0.1% of the injected interstitials were absorbed by the voids, this would correspond to 7×10^4 interstitial/void which is ~2 times higher than the vacancies present in the voids. We conclude that it is possible that the suppression of void formation is caused by the effect of the injected interstitials.

A significant difference in void microstructure is found between single beam and dual beam irradiated microstructures. The void diameter is smaller and the void density is much higher in the latter, indicating that He promotes void formation nucleation, by

increasing the internal gas pressure of the voids which helps stabilize them against vacancy thermal emission [26]. The conclusive effect on the voids therefore appears to be reduction in size with an increment in the concentration which assists swelling as shown in Figs. 10 and 11.

4.3. The RIS behavior in 21Cr32Ni model alloy

Microchemical evolution of Fe, Ni, Cr and Mn is observed near the grain boundaries of the irradiated material. Fig. 12 shows Ni segregation even after 1 dpa with Fe, Cr and Mn depletion along the grain boundaries. The Fe and Cr grain boundary depletion is consistent with previous observations on austenitic stainless steels reported for example by Was et al. [51] and Allen et al. [52], however Mn depletion was not previously reported.

4.4. Temperature shift and comparison of the results with the literature date

It has been shown in the previous sections that the irradiation behavior of the 21Cr32Ni model alloy after single beam and dual beam irradiation can be remarkably different especially in terms of the faulted loop number density and void formation. The introduction of helium increases the densities of both faulted loops and voids with no change in the average diameter of the faulted loops but pronounce reduction of the average void diameter.

In this section, a discussion is given on the application of the temperature shift for the single beam and the dual beam irradiation. For this purpose, the results obtained in this study are compared with data from the literature recently reported for both austenitic stainless steels and alloy 800H irradiated with ions, protons and neutrons at different temperatures [4,6,10,13—15,51,53—58].

Figs. 14—17 shows the densities of faulted loops and voids versus dose as a function of irradiation temperature which is shown with a temperature legend located on the right side of the each figure. Because there is a large collection of data set in the literature,

markers are categorized with respect to type of irradiation for the sake of the discussion given in this section. Specifically, proton irradiation data is shown as circles, while ion/neutron irradiation data is shown a oblique triangles. Up and down triangles represent austenitic and 800H neutron irradiation data, whereas left and right sided triangles represent austenitic and 800H ion irradiation data, respectively. The single beam and dual beam ion irradiation data given in this study are shown with square and diamond markers. These are also shown bolded and with error bars. The single beam and dual beam data plotted in these figures were obtained as follows: The irradiated region (0—2000 nm) is divided into 100 nm width bins and the dose was calculated for each bin as average by using the damage profile obtained from SRIM (Fig. 2). The positions of the loops and the voids are then determined relative to the irradiation surface using a short MATLAB script, so that the depth dependent data can be collapsed into the plots of the number density and average diameter vs. dose shown in these figures. This procedure is applied to each sample. Therefore, single beam results shown in these figures refers to the merged data extracted from the 1, 10 and 20 dpa samples altogether.

Figs. 14 and 15 show that up to 300 °C, the average loop diameter and the loop number density do not change with irradiation dose, regardless of the irradiation particle. This suggests a dynamic steady state in which loops are destroyed and created at the same rate. Between 300 °C and 440 °C, the average faulted loop diameter increases with irradiation temperature as shown in Fig. 14. This could be due to enhanced defect diffusion contributing to loop growth. The increase in the loop diameter in this temperature regime leads to a decrease in the faulted loop population (Fig. 15) likely because of the increase in the loop unfaulting rate from loop growth and impingement of a dislocation. A further increase in the irradiation temperature (500 °C) results in a decrease of the faulted loop density. The faulted loops eventually vanish when irradiation is at 600 °C. An exception to this behavior can be seen in Fig. 15 which shows that the faulted loop population in an 800H sample neutron irradiated at 500 °C is somewhat higher than that seen after ion irradiation at 440 °C. Also, the faulted loop diameter
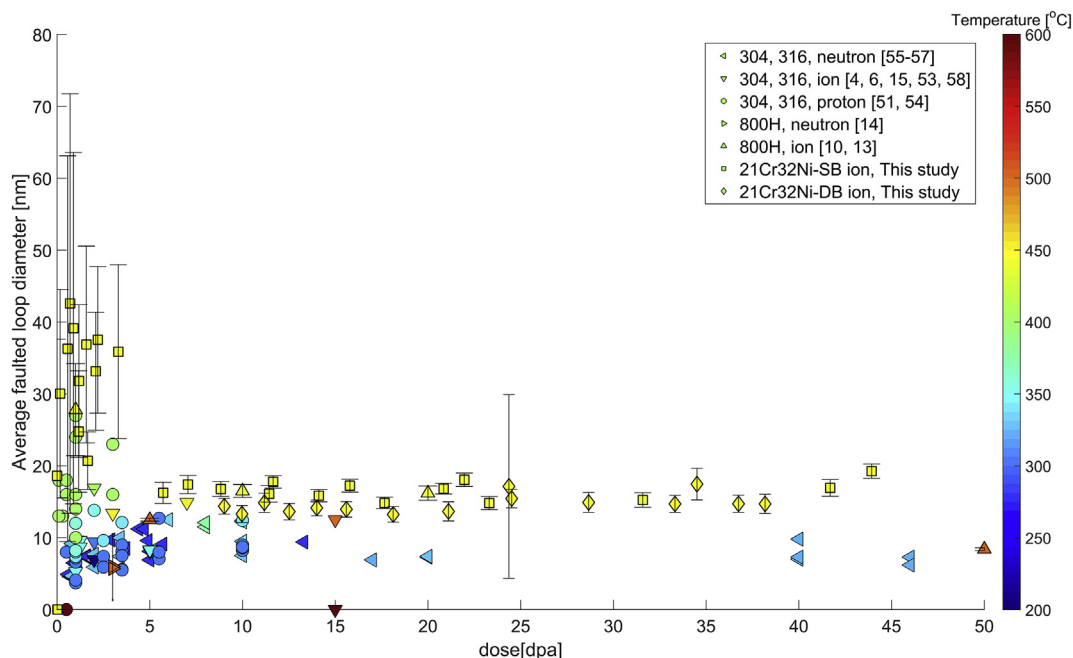

Fig. 14. Comparison of the average faulted loop diameter calculated in this study and the results from the literature for alloy 800H and different austenitic stainless steels irradiated with ions, protons and neutrons [4,6,10,13—15,51,53—58]. (SB: Single-beam, DB: Dual-beam, error bars = ±2 × std.error).
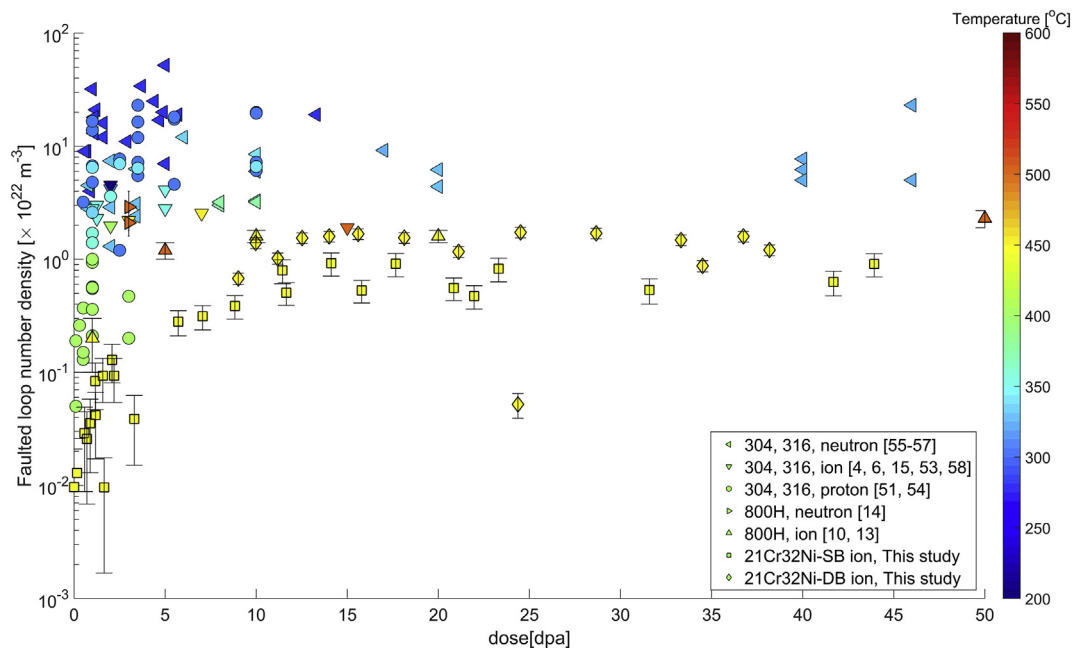
Fig. 15. Comparison of the faulted loop number density calculated in this study and the results from the literature for alloy 800H and different austenitic stainless steels irradiated with ions, protons and neutrons [4,6,10,13–15,51,53–58]. (SB: Single-beam, DB: Dual-beam, error bars = ±2 × std.error).

observed in the alloy 800H neutron irradiated at 500 °C is smaller than seen in the loops studied after ion irradiation of the same alloy at 440 °C. This can possibly be attributed to the higher precipitate density in the neutron irradiated alloy 800H (due to the formation of gamma prime precipitates) than in ion irradiated alloy 800H [10,14]. These additional precipitates can act as recombination sites for point defects and this reduce their influence on the microstructure including absorption at the dislocations. In addition, the high precipitate density observed after neutron irradiation may decrease the unfaulting rate, because they hinder dislocation motion. Further investigation is essential to verify the influence of precipitates on loop evolution in alloy 800H.

Fig. 14 also shows that the average faulted loop diameter in ion irradiated 21Cr32Ni model alloy is in good agreement with the average faulted loop diameter observed in 800H that was irradiated at similar temperature up to 20 dpa. As mentioned previously, the faulted loop diameter is initially large at low doses, but then decreases with dose because of unfaulting and a steady state is immediately reached after ~3 dpa. Also, ion irradiation (with single beam or dual beam) at 440 °C results in similar faulted loop diameter as observed after neutron irradiation of S304/S316 type steels to ~8–10 dpa at 375 °C as predicted by the temperature shift.

Fig. 15 shows that the faulted loop density in ion irradiated model alloys is consistent with values measured in the literature, both for ion and neutron irradiation, that is, it first increases with dose and then saturates after a few dpa. The faulted loop population obtained for the 21Cr32Ni model alloy is a factor of ~2 lower than that seen in alloy 800H. As mentioned above, this can be attributed to the higher unfaulting rate in the model alloy than that seen in alloy 800H. The faulted loop population in the dual beam irradiation is found to be in better agreement with the neutron irradiated austenitic stainless steels at 375 °C than is the faulted loop population seen after the single beam irradiation.

Figs. 16 and 17 show the influence of dose and temperature on the void formation and grwoth. Neutron irradiation of 304 and 316 type stainless steels at low temperature (330 °C) generally results in no void formation, likely due to the low mobility of the defects

created. On the other hand, Edwards et al. reported void formation in neutron irradiated 316 type stainless steel after ~8–9 dpa at 333 °C and 343 °C [55]. This might be due to the difference between the damage rates used in these experiments. The damage rate is higher in ion irradiation which could lead to a relative increase in the defect recombination rate and decrease in void formation and growth.

Fig. 16 shows that the average void diameter and the number density in single beam irradiated 21Cr32Ni model alloy quickly increases and saturates after a few dpa. The average void diameter in the single beam irradiated 21Cr32Ni model alloy is found to be in good agreement with the average void diameter seen in alloy 800H after single beam irradiation to high doses (>10dpa), but not at low doses. In fact, no voids were observed after single beam ion irradiation of alloy 800H below 5 dpa. This indicates that the threshold dose for void nucleation in alloy 800H is higher than that of the 21Cr32Ni model alloy. The void density in the 21Cr32Ni model alloy is slightly smaller than the density seen after single beam irradiation of alloy 800H to 10 and 20 dpa at 440 °C. The reduction in the void density could arise due to the earlier void formation in the model alloy than it is seen in alloy 800H which allows the voids to grow. Still, considering the fluctuations in the data and the large error bars associated with the counting process, this difference is not thought to be significant.

Fig. 16 shows that there is a significant difference in void formation between the dual beam and single beam irradiation of the model alloy at ~440 °C at the doses above 5 dpa. The dual beam results in smaller voids than single beam irradiation, likely as a result of over nucleation. The void diameter is unchanged at doses above 10 dpa similar to what was observed after single beam irradiation as shown in Fig. 16.

Both average void diameter and void number density in the dual beam irradiated 21Cr32Ni model alloy are in better agreement with neutron irradiated data obtained in radiation of austenitic stainless steels at 375 °C or 800H at 500 °C, as compared to single beam irradiation of 21Cr32Ni. Recall that no voids were reported in single beam ion irradiated alloy 800H at 500 °C.
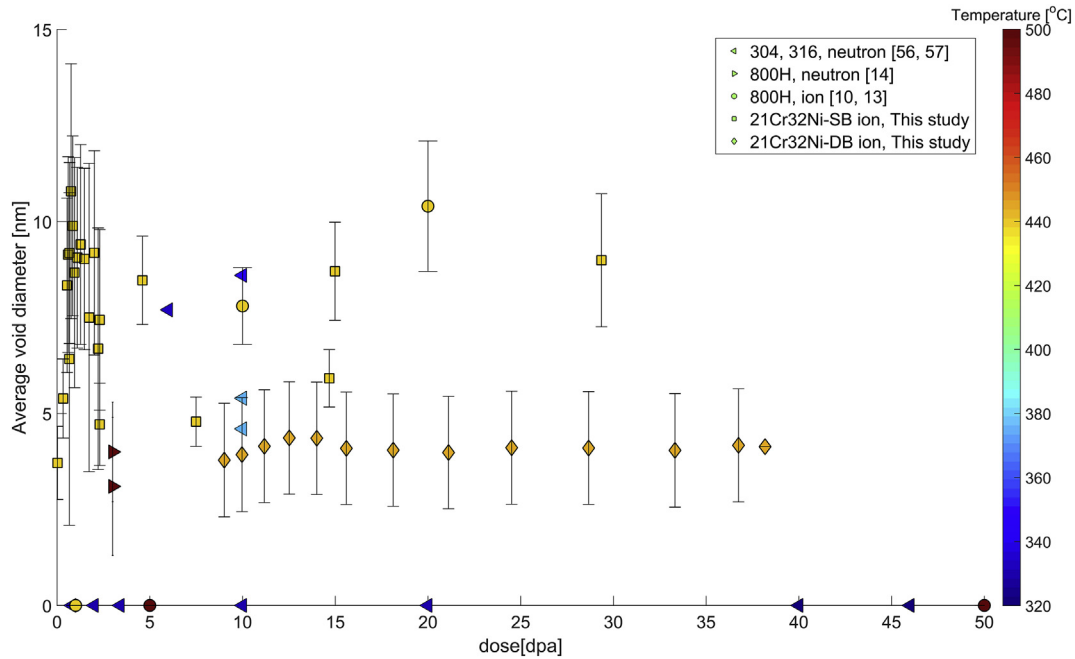
Fig. 16. Comparison of the average void diameter calculated in this study and the results from the literature for alloy 800H and different austenitic stainless steels irradiated with ions and neutrons [10,13,14,56,57] SB: Single-beam, DB: Dual-beam, error bars = ±2 × std.error).
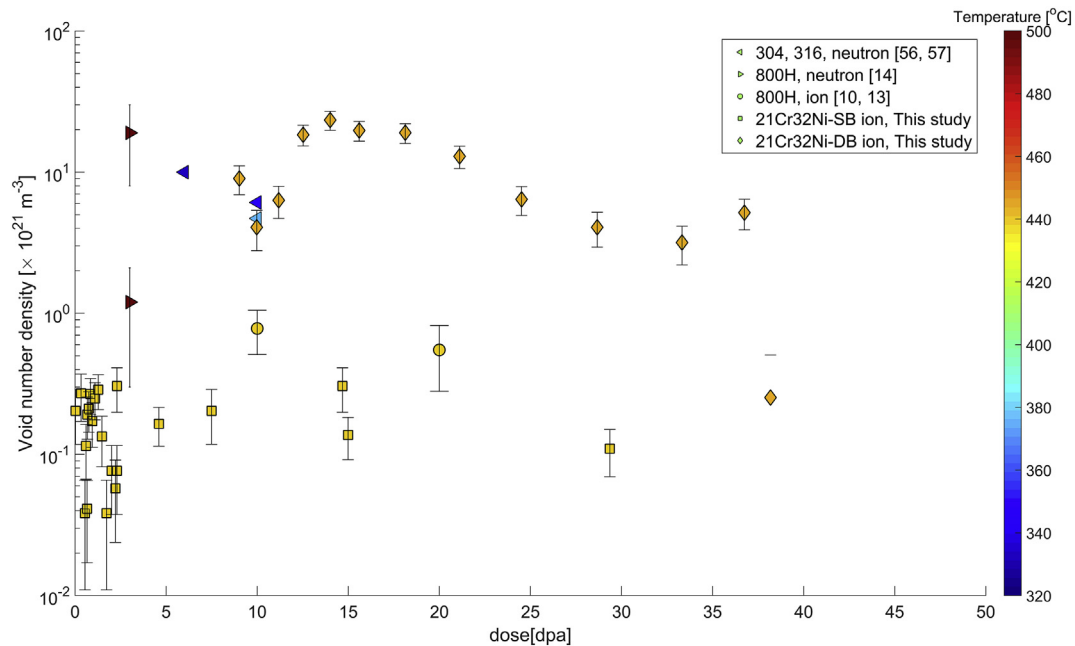

Fig. 17. Comparison of the void number density calculated in this study and the results from the literature for alloy 800H and different austenitic stainless steels irradiated with ions and neutrons [10,13,14,56,57] (SB: Single-beam, DB: Dual-beam, error bars = ±std.error).

These results indicate that the application of the temperature shift during dual beam irradiation improves the match to the microstructures observed after neutron irradiation.

5. Conclusion

In this study, alloy 21Cr32Ni was irradiated with 5 MeV single beam Fe ions and with dual beam where helium is simultaneously injected. The application of the temperature shift to help reproduce the neutron irradiataed microstructure using ions was

demonstrated by irradiating the 21Cr32Ni austenitic model alloy to 1, 10 and 20 dpa with 5 MeV Fe^{++} ions and to 16.6 dpa with Fe and helium at ~440 °C. The evolution of the faulted loop microstructure, void microstructure and radiation induced segregation was investigated and compared. The main conclusions were:

a) Single beam and dual beam irradiation of the 21Cr32Ni model alloy at 440 °C produce faulted loops. The average faulted loop diameter decreases with dose from 1 dpa to 10 dpa, but remains unchanged with further irradiation to 20

dpa. The faulted loop number density increases continuously with dose.

b) In-situ experiments performed with 1 dpa single beam irradiated samples show that the faulted loops can become unfaulted during the irradiation. Unfaulting occurs by the impingement of a dislocation on the loop, as observed during in-situ experiments.

c) The average faulted loop diameter in dual beam irradiated sample to 16.6 dpa at ~440 °C is the same as the average loop diameter obtained after 10 and 20 dpa single beam irradiation at 440 °C. In contrast, the faulted loop density after dual beam irradiation is found to be higher than that found after 10 and 20 dpa single beam irradiation due to the enhanced void nucleation.

d) The calculated average faulted loop diameter vs. dose behavior is in good agreement with similar observations conducted in alloy 800H samples irradiated under similar conditions. However, the faulted loop population in 21Cr32Ni model alloy irradiated with single beam upto 20 dpa is found to be lower than that seen in alloy 800H suggesting that the unfaulting in the model alloy is energetically more favorable and thus unfaulting rate is higher than alloy 800H.

e) Voids were observed both in samples irradiated with single beam and with dual beam. The void diameter is much smaller and the void density is higher more numerous in dual beam as compared to single beam indicating that helium helps void nucleation. Preferential void formation is observed on dislocation lines and grain boundaries. No voids were observed near the irradiated surface of the samples in any of the samples examined in this study, suggesting that in those regions vacancies were lost to the surface.

f) The void distribution in 1 dpa single beam irradiated sample showed a homogenous distribution of voids up to a depth of ~1400 nm, whereas they were only observed near the 1400−2000 nm depth region after doses of 10 and 20 dpa.

g) The average void diameter and number density obtained after irradiation of 21Cr32Ni model alloy with single beam at 440 °C are similar to the same measurements performed in alloy 800H irradiated under the same irradiation conditions.

h) Chemical mapping shows Ni segregation to grain boundaries with Fe, Cr and Mn depletion after only 1 dpa which is consistent with the literature. The degree of segregation increases with dose.

i) The average size and number density of the faulted loops and voids obtained after ion irradiation at 440 °C are consistent with similar values obtained after neutron irradiation of SS304/SS316 type austenitic stainless steels at 375 °C as predicted by Mansur's invariant relations. The overall microstructure of the dual ion beam irradiated sample, where the temperature shift was used, is in good agreement with previously observed neutron irradiated microstructure.

References

[1] B.H. Sencer, et al., J. Nucl. Mater. 414 (2011) 237.
[2] P.J. Maziasz, J.T. Busby, Comp. Nucl. Mater. 2 (2012) 267−283.
[3] G. Was, J. Mater. Res. 30 (9) (2015) 1158−1182.
[4] A. Etienne, et al., J. Nucl. Mater. 400 (2010) 56−63.
[5] D. Chen, et al., Nucl. Instrum. Meth. Phys. Res. B 365 (2015) 503−508.
[6] J. Gupta, et al., J. Nucl. Mater. 501 (2018) 45−58.
[7] Z. Jiao, J. Hesterberg, G.S. Was, J. Nucl. Mater. 500 (2018) 220−234.
[8] T. Kimoto, K. Furuya, H. Shiraishi, J. Nucl. Mater. 179−181 (1991) 507−510.
[9] T. Kimoto, J. Nucl. Mater. 203 (1993) 164−171.
[10] J. Gan, et al., J. Nucl. Mater. 351 (2006) 223−227.
[11] F.A. Garner, W.G. Wolfer, J. Nucl. Mater. 122 (1984) 201−206.
[12] H.R. Brager, F.A. Garner, M.L. Hamilton, J. Nucl. Mater. 133−134 (1985) 594−598.
[13] C. Ulmer, A. Motta, J. Nucl. Mater. 498 (2018) 458−467.
[14] L. Tan, J.T. Busby, H.J.M. Chichester, K. Sridharan, T.R. Allen, J. Nucl. Mater. 437 (2013) 70−74.
[15] Z. Jiao, J. Michalicka and G. Was. 501 (2018) 312−318.
[16] N.H. Packan, K. Farrell, J.O. Stiegler, J. Nucl. Mater. 78 (1978) 143−155.
[17] L.K. Mansur, J. Nucl. Mater. 78 (1978) 156−160.
[18] L.K. Mansur, J. Nucl. Mater. 206 (1993) 306−323.
[19] G. Was, et al., J. Nucl. Mater. 300 (2002) 198−216.
[20] G. Was, et al., J. Nucl. Mater. 456 (2015) 85−98.
[21] K. Asano, Y. Kohno, A. Kohyama, G. Ayrault, J. Nucl. Mater. 157 (1988) 912−915.
[22] A. Kohyama, G. Ayrault, N. Igata, J. Nucl. Mater. 122 (1984) 224−229.
[23] L.K. Mansur, Nucl. Tech. 40 (1977) 5−34.
[24] L.K. Mansur, J. Nucl. Mater. 85−86 (1979) 523−532.
[25] R.E. Stoller, J. Nucl. Mater. 174 (1990) 289−310.
[26] K. Farrell, P.J. Maziasz, E.H. Lee, L.K. Mansur, Radiat. Eff. Defect S 78 (1983) 277−295.
[27] L.K. Mansur, J. Nucl. Mater. 119 (1983) 1−25.
[28] Y. Dai, G.R. Odette, T. Yamamoto, Comp. Nucl. Mater. 1 (2012) 141−193.
[29] S. Hamada, et al., J. Nucl. Mater. 258−263 (1998) 383−387.
[30] N. Yu, et al., Nucl. Instrum. Methods Phys. Res., Sect. A 99 (1995) 566−568.
[31] J.R. Kaschny, et al., Nucl. Instrum. Methods Phys. Res., Sect. A 551 (2005) 200.
[32] E.A. Kenik, J. Nucl. Mater. 85−86 (1979) 659−663.
[33] A. Hishinuma, N.H. Packan, E.H. Lee, L.K. Mansur, J. Nucl. Mater. 122 (1984) 260−265.
[34] E.H. Lee, N.H. Packan, L.K. Mansur, J. Nucl. Mater. 117 (1983) 123−133.
[35] F.A. Garner, W.G. Wolfer, J. Nucl. Mater. 102 (1981) 143−150.
[36] L. Tan, J.T. Busby, J. Nucl. Mater. 443 (2013) 351−358.
[37] K. Yabuuchi, R. Kasada, A. Kimura, J. Nucl. Mater. 442 (2013) S790−S795.
[38] S. Taller, et al., Nucl. Ins. Met. Phys. Sec. B 412 (2017) 1−10.
[39] G. Was, High Fidelity Ion Beam Simulation of High Dose Neutron Irradiation, Integrated Research Project, U. S. DOE, NEUP, Project No. 13-5531, 2013.
[40] J. Ziegler, M.D. Ziegler, J.P. Biersack, Nucl. Instrum. Methods Phys. Res. Sect. B Beam Interact. Mater. Atoms 268 (2010) 1818−1823.
[41] E. Getto, et al., J. Nucl. Mater. 462 (2015) 458−469.
[42] A. Aitkaliyeva, J.W. Madden, B.D. Miller, J.I. Cole, Micron 67 (2014) 65−73.
[43] M.L. Jenkins, Z. Yao, M. Mayoral, M.A. Kirk, J. Nucl. Mater. 389 (2009) 197.
[44] Z. Yao, M. Mayoral, M.L. Jenkins, M.A. Kirk, Phil. Mag. 88 (2008) 2851.
[45] T. Yang, et al., J. Nucl. Mater. 488 (2017) 328−337.
[46] S. Hayakawa, et al., J. Nucl. Mater. Energy 9 (2016) 581−586.
[47] T. Nogaret, C. Robertson, D. Rodney, Philos. Mag. A 87 (2007) 945−966.
[48] A. Kubota, W.G. Wolfer, Mater. Sci. Eng. A 400−401 (2005) 362−365.
[49] A.P. Druzhkov, D.A. Perminov, A.E. Davletshin, J. Nucl. Mater. 384 (2009) 56−60.
[50] F.A. Garner, A.S. Kumar, ASTM STP 55 (1987) 289−314.
[51] G. Was, et al., J. Nucl. Mater. 270 (1999) 96−114.
[52] T.R. Allen, J.T. Busby, G.S. Was, E.A. Kenik, J. Nucl. Mater. 255 (1998) 44−58.
[53] H. Jin, et al., J. Nucl. Mater. 493 (2017) 239−245.
[54] B.H. Sencer, et al., J. Nucl. Mater. 323 (2003) 18−28.
[55] D.J. Edwards, et al., J. Nucl. Mater. 317 (2003) 13−31.
[56] D.J. Edwards, F. Garner, E. Simonen, S. Bruemmer, Characterization of Neutron-irradiated 300-Series Stainless Steels to Assess Mechanisms of Irradiation-assisted Stress Corrosion Cracking: vol. 2: Core Components 1001497, EPRI, Palo Alto, CA, 2001.
[57] C. Pokor, et al., J. Nucl. Mater. 325 (2004) 19−29.
[58] S. Jublot-Leclerc, et al., J. Nucl. Mater. 480 (2016) 430−446.